



Surface chemistry and porosity engineering through etching reveal ultrafast oxygen reduction kinetics below 400 °C in B-site exposed (La,Sr)(Co,Fe)O₃ thin-films

Matias Acosta^{a,*}, Federico Baiutti^b, Xuejing Wang^c, Andrea Cavallaro^d, Ji Wu^e, Weiwei Li^a, Stephen C. Parker^e, Ainara Agüero^d, Haiyan Wang^c, Albert Tarancón^{b,f}, Judith L. MacManus-Driscoll^a

^a Department of Materials Science and Metallurgy, University of Cambridge, 27 Charles Babbage Road, Cambridge, CB3 0FS, UK

^b Catalonia Institute for Energy Research (IREC), Department of Advanced Materials for Energy, 1 Jardins de les Dones de Negre, Barcelona, 08930, Spain

^c School of Materials Engineering, Purdue University, 701 West Stadium Avenue, West Lafayette, 47907-2045, USA

^d Department of Materials, Imperial College London, SW7 2AZ, UK

^e Department of Chemistry, University of Bath, Claverton Down, Bath, BA2 7AY, UK

^f ICREA, 23 Passeig Lluís Companys, Barcelona, 08010, Spain

HIGHLIGHTS

- LSCF and LSCF-MgO are etched to study oxygen exchange kinetics.
- The roles of surface topography and chemistry on oxygen exchange are investigated.
- Etching removes Sr-excess, exposes B-site cations & increases 200% LSCF-MgO surface.
- Etching results in reduced activation energy from 1 eV to 0.4 eV.
- Etching enhances oxygen exchange kinetics by an order of magnitude.

ARTICLE INFO

Keywords:

Mesoporous materials
Oxygen reduction
Solid oxide cell cathode
Nanoscale oxide
Surface tuning
Surface modification
Thin-films

ABSTRACT

Oxides are critical materials for energy devices like solid oxide cells, catalysts, and membranes. Their performance is often limited by their catalytic activity at reduced temperatures. In this work, a simple etching process with acetic acid at room temperature was used to investigate how oxygen exchange is influenced by surface chemistry and mesoporous structuring in single-crystalline epitaxial (La_{0.60}Sr_{0.40})_{0.95}(Co_{0.20}Fe_{0.80})O₃. Using low energy ion scattering and electrical measurements, it is shown that increasing the B-site transition metal cation surface exposure (most notably with Fe) leads to strongly reduced activation energy from $E_a \approx 1$ eV to $E_a \approx 0.4$ eV for oxygen exchange and an order of magnitude increased oxygen exchange kinetics below 400 °C. Increasing the active area by ~200% via mesoporous structuring leads to increased oxygen reduction rates by the same percentage. Density functional calculations indicate that a B-site exposed surface with high oxygen vacancy concentration can explain the experimental results. The work opens a pathway to tune surfaces and optimize oxygen exchange for energy devices.

1. Introduction

Solid oxide cells (SOCs) are among the most efficient clean energy conversion technologies. They can use many different fuels and be built in micrometer or large scale with excellent modularity [1–3]. At the

micrometer-scale (i.e., in micro-SOC), they offer a large energy density that makes them attractive to replace batteries in high-power consumer products. Despite their significant advantages, SOC's are not widely implemented owing to their high operating temperature (>700 °C), and there are also cost and reliability issues. Lowering their operational

* Corresponding author.

E-mail address: ma771@cam.ac.uk (M. Acosta).

<https://doi.org/10.1016/j.jpowsour.2022.230983>

Received 20 October 2021; Received in revised form 23 December 2021; Accepted 6 January 2022

Available online 22 January 2022

0378-7753/© 2022 Elsevier B.V. All rights reserved.

temperature results in high ohmic resistance at the electrolyte and high polarization resistance, especially at the cathode. The former can be overcome by developing thin-film electrolytes, while the latter is much more challenging and requires an increase in oxygen exchange kinetics at reduced temperature. Indeed, the sluggish kinetics for oxygen reactions at the cathode is the greatest challenge for reducing the SOC's operational temperature [1,3–5].

Perovskite materials like (La,Sr)(Co,Fe)O₃ (LSCF) and (La,Sr)CoO₃ (LSC) have been widely investigated for SOC cathodes because of their high ionic and electronic conductivities, both of which are required for good cathode performance. The surface nanostructure and surface chemistry/crystal structure of cathodes also play critical roles in oxygen exchange, and they have been extensively studied to improve their performance [5–10]. It is generally accepted that increased porosity or roughness favors oxygen exchange due to an extended surface and increased reaction area [9,11,12]. Recent works, however, shed light on other key considerations to improve cathode performance. Different surface crystallographic planes [8], cations with different reducibility at the surface [7], or different oxide phases at the surface [7,13–15] can modify oxygen exchange kinetics dramatically. Also, it has been theoretically shown that B-site terminated surfaces can feature two to three orders of magnitude faster oxygen exchange kinetics than A-site terminated ones [5].

When thinking about chemical surface engineering, one should also consider that perovskites suffer from Sr²⁺ surface segregation, which is known to be detrimental to catalytic and transport properties because of the formation of dielectric phases like SrO, reconstructed Sr-excess phases (SrO-nABO₃), or reaction products following the SrO reactivity with chemisorbed gas species (i.e., Sr(OH)₂ or SrCO₃) [16–19]. Cation diffusion kinetics in perovskites and the concomitant detrimental formation of Sr-excess phases becomes particularly acute above 450 °C [5, 15,17,20]. This provides an upper limit for operating a perovskite cathode with an acceptable degradation between 5% and 10% for operation times of 10 000 h [20]. However, developing cathodes working at such low temperatures has not been possible due to the low oxygen exchange kinetics that leads to high polarization losses. This highlights the need for novel nanostructured materials with a high catalytic activity that can work at reduced temperatures.

In this work, model heteroepitaxial films of (La_{0.60}Sr_{0.40})_{0.95}(Co_{0.20}Fe_{0.80})O_{3-δ} (100LSCF) and vertically aligned nanocomposite (VAN) heteroepitaxial films of 50 wt % LSCF +50 wt % MgO (50LSCF-50MgO) were investigated. In the case of the VAN films, simple etching allows the removal of MgO (readily soluble in mild acids) from the LSCF matrix, rendering mesoporous thin-film LSCF cathodes with a maximized surface area for solid/gas reactions. Moreover, by comparing this material with an equally etched single-phase LSCF film in which only the surface chemistry is altered (not the surface nanostructure), it was possible to highlight an additional important effect on the oxygen reduction kinetics caused by a change in the surface chemistry upon etching. This allows us to distinguish the surface nanostructure and chemistry roles on the surface exchange kinetics. It is shown that surface area increases oxygen exchange proportionally to the increased geometrical factor. In contrast, modifying the surface chemistry leads to substantial changes in the electrochemical properties. Particularly, it is observed that surface chemistry dramatically reduces the oxygen exchange activation energy and significantly increases its kinetics. Hence, it is found that an increase in oxygen exchange kinetics by more than one order of magnitude at temperatures ranging between 300 °C and 500 °C, and the activation energy for oxygen reduction decreases from ≈1 eV to ≈0.4 eV. At the same time, it is shown from surface chemical analysis that chemical etching exposes an increased concentration of B-site cations (particularly Fe) at the surface. Furthermore, the experimental findings are supported by Density Functional Theory (DFT) calculations which show that a B-site (specifically Fe) exposed films with surface defects, namely a high local concentration of oxygen vacancies, can explain the low activation energies experimentally measured.

2. Experimental section

The first step for producing the PLD thin-films is to synthesize the bulk targets with appropriate chemical composition. The targets were produced using commercial ceramic powders with the stoichiometry (La_{0.60}Sr_{0.40})_{0.95}(Co_{0.20}Fe_{0.80})O₃ (LSCF) (Fuel cell materials, Nexceris, LLC) and MgO (99.95% purity, Alfa Aesar Ltd). Disk-shape samples of 12 mm in diameter and 2 mm thick (80 mg of powder) were uniaxially pressed (Perkin-Elmer) at 800 MPa for 180 s. After that, they were cold isostatically pressed (Stansted Fluid Power Ltd) at 150 MPa for 180 s to produce the targets for pulsed laser deposition (PLD). The green bodies obtained were sintered in covered alumina crucibles with atmospheric powder at 1300 °C for 4 h and a heating rate of 5 °C/min. Sintered pellets were ground before each deposition manually with a 1200 grid grinding paper. Targets with compositions corresponding to 100 wt % LSCF-0 wt % MgO (100LSCF), 75 wt % LSCF-25 wt % MgO (75LSCF-25MgO), and 50 wt % LSCF-50 wt % MgO (50LSCF-50MgO) were produced. As will become apparent throughout the manuscript, the targets with a mixture of LSCF and MgO are used to synthesize the self-assembled VAN comprised of LSCF nanowalls and MgO nanopillars.

Using these bulk targets, LSCF and VAN thin-films were grown on two substrates, (001) Nb-doped SrTiO₃ and (001) 0.3(LaAlO₃)-0.7 (Sr₂TaAlO₆) (LSAT). The substrates were chosen because they have little lattice mismatch (lower than 0.2%) with the thin-films investigated in this manuscript, and so the films should grow with high crystallinity. Before each deposition, the PLD chamber was evacuated to a base vacuum of at least 1.3×10^{-5} mbar. The oxygen partial pressure during the deposition was kept at 0.4 mbar. The deposition temperature of the thin-films was optimized for each substrate independently. Single crystalline and epitaxial films were obtained at 750 °C for (001) Nb-doped SrTiO₃ and at 800 °C for (001) LSAT. A KrF excimer laser (Lambda Physik, Inc) with a wavelength of 248 nm was focused on the target for the deposition. The laser energy density and frequency were kept constant at 0.5 J/cm² and 3 Hz, respectively. The target-substrate distance was fixed at 45 mm. The deposition rate for the thin-films and VAN was 0.003 nm per pulse. Subsequently, thin-films were investigated in the as-grown state, etched at room temperature state, and 'etched + annealed' state. For the latter, the samples were annealed at 450 °C for 4 h. The etching was done by immersing the VAN in 20 vol % acetic acid while stirring the solution for 5 min, 10 min, 15 min, and 17 min. Throughout the manuscript, it is indicated whether the results are presented for the as-grown, etched or 'etched + annealed' states.

Several characterization techniques were used to analyse the samples. Firstly, X-ray diffraction was done in a high-resolution X-ray diffractometer using Cu Kα1 radiation ($\lambda = 1.5405 \text{ \AA}$) (Malvern Panalytical, Spectris plc). The θ -2 θ scans were done in the angular range between 15° and 120° with a step size of 0.01° and counting time of 0.4 s/step. Atomic force microscopy (Multimode 8, Bruker Ltd) was done in the tapping mode. Commercial Silicon cantilevers (Budget sensors Ltd) were used for all measurements, which had a nominal spring constant of 40 N/m and a resonance frequency of 300 kHz. Images were acquired with a lateral resolution of (256 × 256) pixels and a frequency of 1 Hz. Scan areas between (1.0 × 1.0) μm² and (5.0 × 5.0) μm² were measured in several points of the samples. Topographic images were processed using line flattening or median of differences to remove the effect of the surface tilt and drifts. The reduction of MgO content with etching time was estimated by considering the integrated area of the (002) peaks following each etching step.

Secondly, X-ray photoelectron spectroscopy was undertaken using a monochromatic Al Kα1 radiation ($h\nu = 1486.6 \text{ eV}$) using a SPECS PHOIBOS 150 electron energy analyser with a total energy resolution of 500 meV. To remove the charging effect during the measurements, a low-energy electron flood gun with proper energy was applied. All spectra were aligned to the C 1s at 284.8 eV. To evaluate further the chemical composition of the first atomic layer of the samples, a Low Energy Ion Scattering (LEIS) technique was employed [21]. A Qtac100

LEIS instrument (ION-TOF GmbH) operating with three different primary ions (helium, neon or argon) and equipped with a Hyperion high brightness primary ion source (Oregon Physics, USA) was employed. Neon primary ion beam was preferred for its higher mass resolution between Fe and Co and the higher sensitivity to the elements in this mass range. In the first atomic layer surface analysis, Ne⁺ 5 keV was rastered on a sample area of 500 μm × 500 μm. The energy range was maintained in 1000–3100 eV range. The total Ne⁺ dose was kept around 5 × 10¹³ ions/cm². For the calibration and error calculation, a PLD dense LSCF target of known stoichiometry was snapped in two pieces and Ne⁺ LEIS analysis was performed on the fresh LSCF surface.

Thirdly, scanning electron microscopy (SEM, FEI Nova NanoSEM FEG) measurements were done in as-grown samples. The images obtained were used to calculate the surface area of the samples. Image analysis using ImageJ2 [22] allowed us to obtain the porous fraction of the samples and the perimeter of the porous. Using the thickness of the nanocomposites and perimeter of the porous nanostructure, it was possible to estimate the increase in surface area as a function of etching time in all samples.

To conclude the surface characterization, bright-field TEM images, HAADF STEM, selected area electron diffraction (SAED) patterns, and energy-dispersive X-ray spectroscopy (EDS) chemical mapping were acquired by the FEI Talos F200X TEM. The TEM samples were prepared using a standard cross-section sample preparation procedure, including manual grinding, polishing, dimpling, and an ion milling step (PIPS 691 precision ion polishing system, 4.0 keV).

Upon concluding the structural and surface characterization, electrochemical characterization was made. DC conductivity relaxation was measured on 100LSCF, 75LSCF/25MgO, and 50LSCF/50MgO thin-films grown on LSAT because of the substrate's large resistivity. A 4 point-probe Van der Pauw configuration and also a 4 point surface resistance with strip current collectors were done using painted Au contact pads in a HT-Linkam setup (chamber volume ≈ 20 cm³). Since results were almost identical, all results are shown in etched + annealed samples with Van de Pauw electrodes. Conductivity relaxation experiments were carried out between synthetic air and O₂ using a gas flow of ≈ 150 cm³/min directly conveyed on the film surface. The estimated flushing time is < 6s, as retrieved by utilizing a fast-reacting sample in the sensor regime [23]. The reported relaxation time constant for each temperature step is the average of at least 2 full gas exchange cycles.

Lastly, to complement the experimental findings, theoretical calculations were made using the density functional theory method with a linear combination of atomic orbitals (LCAO) to simulate the oxygen reduction reactions at La_{0.5}Sr_{0.5}Fe_{1-β}O_{3-δ} surfaces at 0 K was used. The calculations were carried out with the CRYSTAL17 software package [24]. The hybrid HSE06 functional was used to properly account for the strong electron correlation in the Fe-containing oxides. The computational models were visualized with the DLV package throughout this work [25]. The electrons in Sr, Fe, La, and O atoms are described with double-zeta polarised basis sets, which are proven to describe these species in perovskite oxides well [26,27]. Particularly, the La basis sets contain a quasi-relativistic core pseudopotential to approximate the relativistic behaviors of La core electrons [28].

Initial bulk La_{0.5}Sr_{0.5}Fe_{1-β}O_{3-δ} lattice was constructed as a 2 × 2 × 2 supercell (40 atoms) from the experimental unit cell. The structures with symmetrically unique orderings of the A-site La and Sr atoms are scanned with the Supercell program [29]. The lattice with the lowest electrostatic energy was then relaxed at the DFT level with spin-polarization and periodic boundary condition, and anti-ferromagnetic ordering was applied to the Fe atoms. The Coulombic and exchange series were summed to the cut-off thresholds of 7, 7, 7, 7, and 14 as detailed in the CRYSTAL17 manual. A Monkhorst-Pack k-point mesh with a shrinking factor of 4 was used for all models except for the slab calculations, where the shrinking factor in the z-direction was reduced to 1. The lattice relaxation steps were considered as converged when the energy difference between iterations was smaller than 10⁻⁷ Hartree.

The surface models were constructed by cleaving the relaxed bulk lattice at the Fe-terminated (001) plane. The pristine slab contained 6 layers of atoms (60 atoms). The Fe-terminated surfaces were taken as the reaction surfaces to be studied, and two bottom layers were fixed during relaxation to represent the bulk solid. An equivalent of 500 Å vacuum layer was applied in the z-direction to eliminate any possible slab-slab interactions. Two different defective Fe-terminated surfaces were then prepared by removing two O atoms and removing 4 O atoms and one Fe atom together from the relaxed pristine slab model, respectively. The transition states of the oxygen dissociations at the relaxed oxygen vacancy sites on each of these surfaces were then searched using the Distinguished Reaction Coordinates (DRC) method available in the CRYSTAL17 package [30].

3. Results

The results on heteroepitaxial films of 100LSCF and 50LSCF-50MgO, before and after chemical etching were compared. This enables us to distinguish the separate roles of surface chemistry and LSCF surface area on oxygen exchange kinetics. It is worth noting that by *surface chemistry* cations and anions at the first atomic layer of the surface are being referred to, whereas by the *surface area surface topography* (i.e. porous or non-porous surface) exposed to the measurement atmosphere is being referred to. Throughout the manuscript, it will become clear that the chemical etching process only modifies the surface chemistry of 100LSCF, whereas it modifies *both* surface chemistry and surface area in 50LSCF-50MgO films. For the latter films, MgO nanopillars in the VAN films are etched out leaving a mesoporous film consisting of percolated nanowalls of LSCF. Firstly, the data on phase epitaxial relationships, microstructures, crystallographic phases, and surface chemistries are presented, followed by data and calculations on the surface oxygen reaction kinetics.

The crystallographic data for the 100LSCF and the 50LSCF-50MgO films is introduced in Fig. 1. Fig. 1a shows θ-2θ X-ray diffraction (XRD) pattern of 100LSCF and 50LSCF-50MgO. Both sets of films are of ~70 nm thickness and they are grown on (001) (LaAlO₃)_{0.3}(Sr₂AlTaO₆)_{0.7} (LSAT) single crystal substrates. This substrate was chosen because of its low lattice match with LSCF (lattice mismatch 0.13%) and its high resistivity, making electrical relaxation experiments possible (shown later in the manuscript). The XRD pattern for 100LSCF shows four major peaks at 22.8°, 46.5°, 72.6°, and 104.6°. The peaks correspond to (002) orientations of LSCF. The XRD pattern for 50LSCF-50MgO shows the same (002) orientations of LSCF. Two high-intensity peaks at 43° and 94.5° are also observed corresponding to MgO (002). A low-intensity peak at 62.5° corresponds to the MgO (022) [31]. A small content of MgO oriented along (022) in 50LSCF-50MgO grown on LSAT is observed.

Fig. 1b shows a schematic nanostructure of an as-grown 50LSCF-50MgO VAN film consisting of a percolated LSCF matrix and MgO nanopillars. TEM data in Fig. 2 confirm this microstructure. The surface topography of the as-grown VAN film obtained using atomic force microscopy (AFM) is also shown in Fig. 1b. A very smooth film with RMS roughness of only 1.02 nm is obtained. The MgO pillars are seen intersecting the film surface.

The 50LSCF-50MgO VAN films were etched to remove the MgO nanopillars. The simple process was done by immersing them in 20 vol% acetic acid while stirring the solution at room temperature. As indicated in Fig. S1, etching for 15 min or more renders a MgO content below the XRD detection limit for the 70 nm thickness VAN (this result is also supported later on by transmission electron microscopy). The fully etched films have an increase in out-of-plane lattice parameter of the LSCF phase from (3.898 ± 0.001) Å to (3.906 ± 0.002) Å (i.e., a 0.2% out-of-plane strain). This indicates that the MgO in the as-grown VAN films imposes a compressive out-of-plane strain in the LSCF constituent of the 50LSCF-50MgO during growth. As shown later, this strain effect has no considerable influence on the enhanced oxygen exchange kinetics

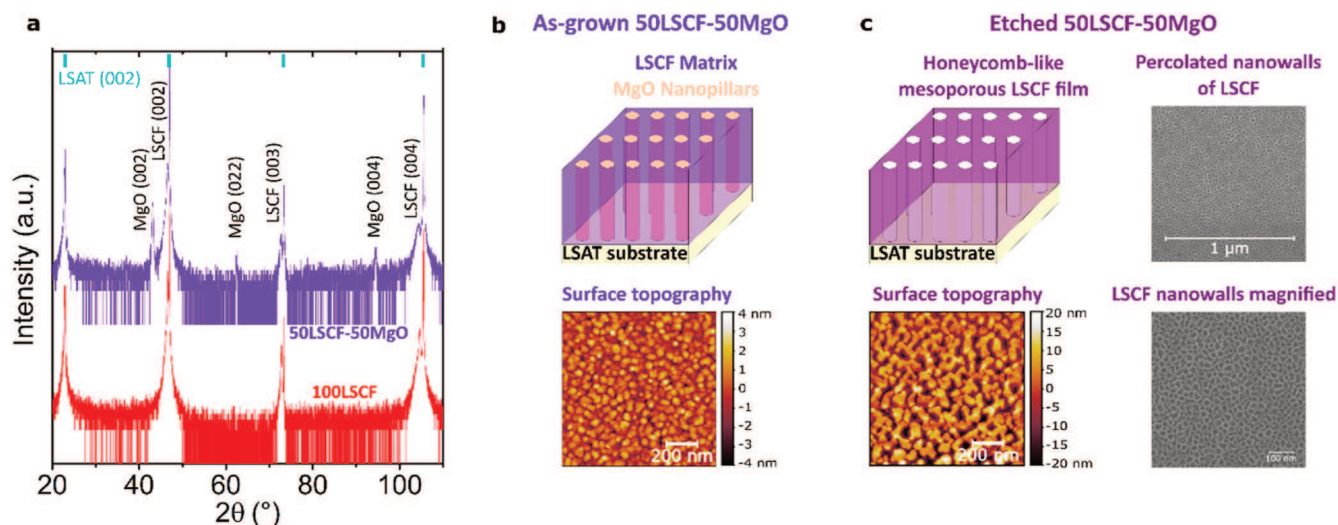
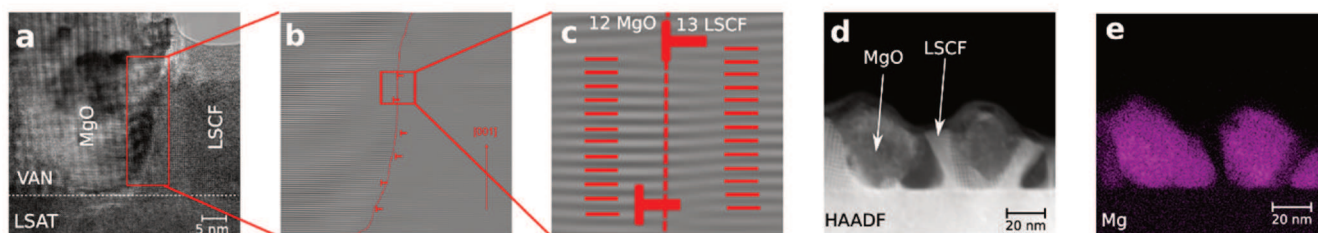


Fig. 1. (a) XRD pattern of 50LSCF-50MgO and 100LSCF grown on LSAT. (b) Schematic representation of as-grown 50LSCF-50MgO VAN and its surface topography obtained by AFM. (c) Schematic representation of fully etched 50LSCF-50MgO VAN, its surface topography obtained by AFM, and scanning electron microscopy images (SEM) low and high magnification. The slight modification of the purple colour of the etched VAN film is purposely made to emphasize a change in the surface topography and surface chemistry upon etching. (For interpretation of the references to colour in this figure legend, the reader is referred to the Web version of this article.)

As-grown 50LSCF-50MgO



Etched 50LSCF-50MgO

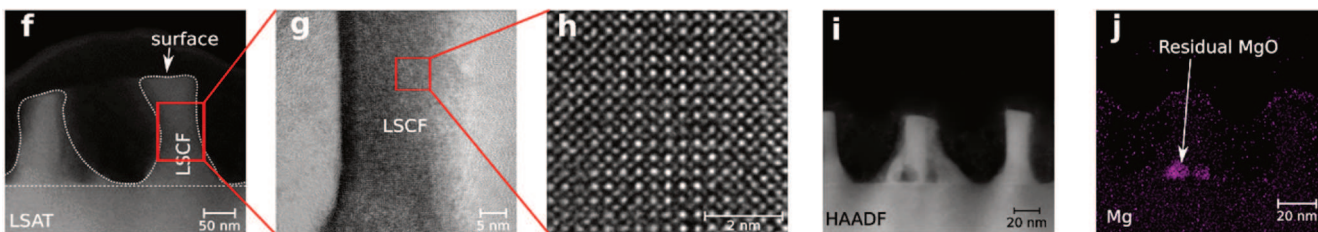


Fig. 2. (a) and (f) show a TEM image of the cross-section of as-grown 50LSCF-50MgO and etched 50LSCF-50MgO, respectively. (b) and (g) are magnifications of the out-of-plane interface region and LSCF nanowall in as-grown 50LSCF-50MgO and etched 50LSCF-50MgO, respectively. (c) shows a high magnification of (b), indicating an out-of-plane domain matching of 13LSCF:12MgO. (h) shows a high magnification of the LSCF perovskite lattice in the etched 50LSCF-50MgO. (d) and (i) HAADF show an image of a magnified cross-section of as-grown 50LSCF-50MgO and etched 50LSCF-50MgO, respectively. (e) and (j) show an EDS map of the Mg content for the as-grown 50LSCF-50MgO and etched 50LSCF-50MgO, respectively.

of the LSCF.

Fig. 1c shows a schematic of a fully etched film. The sketch was made using a different purple colour from the as-grown sample to highlight the change in the surface topography and the surface chemical composition discussed later. The AFM image shows a percolated single-crystalline honeycomb-like mesoporous LSCF film after complete etching out of the MgO. By doing image analysis (using ImageJ2 [22]) over a $5 \times 5 \mu\text{m}^2$ area, the relative porosity is determined to be 46% and the mean pore size to be 64 nm for the etched 50MgO-50LSCF. Importantly, as seen from the scanning electron microscopy (SEM) image in

Fig. 1c, it is possible to observe that a honeycomb-like mesoporous LSCF film was successfully synthesized. In other words, etching out MgO from the VAN films leads to a mesoporous film consisting of percolated nanowalls of LSCF that span uniformly over a large surface area of several square microns. In fact, by scanning across the whole film, a similar pattern was observed. Hence, the process produces a uniform honeycomb over $5 \text{ mm} \times 5 \text{ mm}$. Several honeycomb-like mesoporous LSCF nanostructured films can be synthesized by varying the substrate and VAN composition, i.e. % of MgO in the VAN film. Fig. S2 shows four exemplary mesoporous nanostructures that feature a different

morphology of nanowalls of LSCF. By varying such parameters, a tuning of the surface morphology (pore size from ≈ 2 nm to ≈ 60 nm) can be achieved. Most importantly, MgO etching leads to a significant enhancement of the surface area (between $\approx 200\%$ and $\approx 500\%$), for films that are, in all cases, as thin as 70 nm. Table S1 shows a detailed quantitative analysis of the surface morphology, which is consistently reproducible over large surface areas. For the rest of the paper, the focus is the already-described 50LSCF-50MgO VAN film on LSAT and its properties are compared to 100LSCF.

Fig. 2 shows transmission electron microscopy (TEM) images and chemical analyses of the 50LSCF-50MgO VAN films. Particularly, Fig. 2a shows cross-section transmission electron microscopy (TEM). A clean interface is observed with Moiré patterns and/or thickness fringes present (the electron beam is not perpendicular to the interfaces through the whole film thickness leading to overlapped lattices of LSCF and MgO). Fig. 2b shows a magnified STEM cross-section image of the interface between LSCF and MgO. The image reveals a clean interface between the LSCF and the MgO. Detailed investigation of out-of-plane heterointerfaces (Fig. 2c) allowed us to determine the domain matching epitaxy (DME) relation of $12\text{MgO}:13\text{LSCF}$. Fig. 2d shows a cross-section of the VAN that was further analysed by high-angle annular dark-field (HAADF) imaging. Different contrast was observed between the LSCF and MgO due to the phases' different average atomic numbers. Energy-dispersive X-ray spectroscopy (EDS) corroborates the presence and distribution of the MgO phase within the VAN (Fig. 2e) without any Mg in the LSCF phase, within the detection limits.

Fig. 2f shows a low-magnification cross-section STEM image of the 15 min etched 50LSCF-50MgO VAN. The mesoporous LSCF film shows nanowall features in the cross-section view. These features are consistent with the percolated honeycomb-like mesoporous nanostructure formed over large areas (Fig. 1). Fig. 2g and h show high magnification images of an LSCF nanowall region near its vertical surface. The images reveal that the LSCF matrix remains a structurally intact perovskite phase after etching. Fig. 2i shows a cross-section HAADF micrograph. In contrast to Fig. 2d, no MgO is present in Fig. 2i. EDS analysis (Fig. 2j) reveals only very minor residual MgO at the base of the film in small regions. Hence, there is only trace MgO remaining in the etched film. More detailed images of the MgO and LSCF crystalline structure, as well as distribution of all chemical elements for both as-grown and etched 50LSCF-50MgO, are shown in Supplementary S3.

To evaluate the surface chemistry at relevant working conditions, samples were investigated in as-grown state, etched at room temperature, and 'etched + annealed' state in which samples were annealed at 450 °C for 4 h. The annealing conditions were chosen to represent a typical operational temperature expected for cathodes in micro-SOFC and considering the metastability of similar perovskites reported

elsewhere [15]. It was observed that the 'etched + annealed' surfaces were stable at the tested temperatures for over 8 h. Longer-term stability studies were out of the scope of this work, however, it will be further investigated in future works.

To determine whether etching had any influence on the surface chemistry of the mesoporous LSCF film (after 15 min etching 50LSCF-50MgO), low energy ion spectroscopy (LEIS) was performed. LEIS is very sensitive to the first atomic layer of the surface. The technique and any measurement errors are described in detail in the experimental procedure and explained in more detail elsewhere [21]. In brief, Ne ions were rastered over the sample surface with a perpendicular angle to it to probe its composition (the LEIS intensity of each atom species is directly proportional to its concentration). The stoichiometries were calculated by first calibrating the Ne primary ion yield concerning the LSCF elements, analysing de facto a LSCF "fresh" cleaved surface with known stoichiometry as a reference. More details are described in the experimental section.

Fig. 3a shows the stoichiometry of La, Sr, Co, Fe species present at the 50LSCF-50MgO surface for the as-grown, etched, and 'etched + annealed' samples at 450 °C for 4 h. The cation contents for the individual cations for bulk stoichiometric LSCF are shown as horizontal dashed lines.

In the as-grown state, a very high relative content of Sr at the surface was observed, which is expected owing to well-known Sr segregation effects arising from the high-temperature growth (Fig. 3a) [16,17]. In other words, the B-site cations at the surface are low in content owing to this Sr-surface enrichment. Notably, there is a low Co content of the LSCF composition which is close to the detection limit of the LEIS technique, limiting the possibility of an accurate Co quantification. For this reason, only the surface Co concentration trend between different samples is discussed. Such Sr-riched and Co-depleted surfaces have been reported elsewhere [12,13].

After etching to produce the etched data in Fig. 3 (a), a considerable decrease in the Sr surface content from (54 ± 4) at. % to (34 ± 4) at. % (Sr is etched-out by mild acids [12]) was observed. Unsurprisingly, therefore, all the other cation contents (La, Co, Fe) increase with etching (La from (28 ± 4) at. % to (64 ± 4) at. %, Co from a concentration below the detection limit to (8 ± 15) at. %, and Fe from (10 ± 5) at. % to (29 ± 5) at. %).

Subsequent annealing procedure that results in the 'etched + annealed' material led to a relatively minor increase in the surface content of La (from (64 ± 4) at. % to (68 ± 4) at. %), a substantial increase in the content of Fe (from (29 ± 5) at. % to (60 ± 5) at. %), as well as almost no variation in the contents of Co (from (8 ± 15) at. % to (9 ± 15) at. %) or Sr (from (34 ± 4) at. % to (32 ± 4) at. %). Hence, with annealing, the Fe content increases markedly at the surface to double the

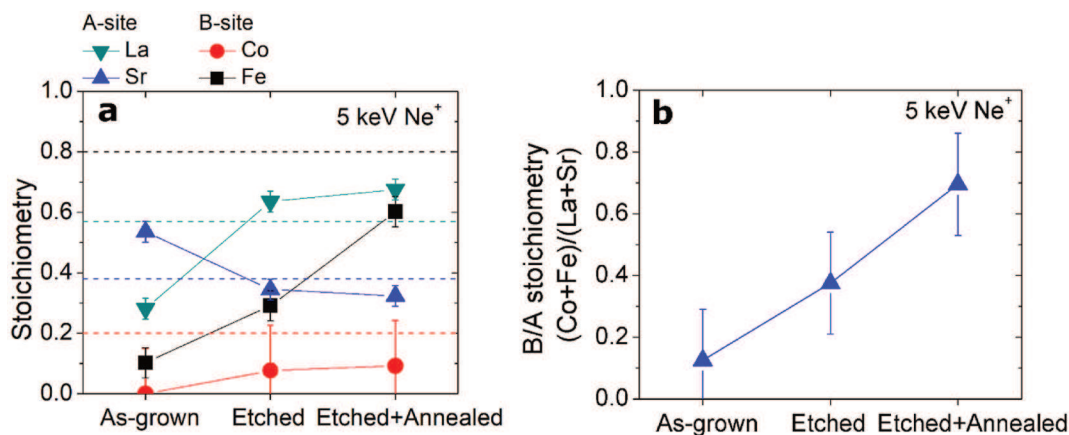


Fig. 3. (a) Surface chemical stoichiometry quantified using LEIS for 50LSCF-50MgO as-grown, etched, and etched + annealed states. The dashed horizontal lines indicate the stoichiometric values of the target. (b) B to A stoichiometric ratio obtained by LEIS for the as-grown, etched, and etched + annealed states.

value of the etched film while the other cation contents change little and thus, there is preferential enrichment of Fe at the surface under our annealing conditions (450 °C for 4 h). The changes with annealing conditions at the surface chemistry imply a thermally activated surface diffusion that is consistent with other work in similar thin-film perovskites that show that annealing at similar conditions (albeit at a higher temperature of 600 °C cf. our 450 °C anneal) is sufficient to thermally activate surface cation diffusion [15].

It is noted that the ‘etched + annealed’ material has a near stoichiometric A-site (La + Sr) cation, i.e. comparing measured vs. nominal compositions, respectively. The A-site cation content values are (68 ± 4) at.% cf. 57 at.% La, and (32 ± 4) at.% cf. 38 at.% Sr, and so La + Sr measured is (100 ± 6) at.% cf. 95% nominal. In contrast, even though the B-site (Co + Fe) surface contents increase after the etching and annealing process, they remain lower than the nominal content. The same comparative values are (9 ± 5) at. % cf. 0 at. % Co, and (60 ± 5) at. % cf. 80 at. % Fe, and so Co + Fe measured is (69 ± 16) at.% cf. the 100% nominal. Therefore, the lower Co and Fe surface content compared to the nominal one suggests B-site sub-stoichiometry at the film surface, but a substantial Fe surface exposure level increase.

Fig. 3b shows the relative surface intensities of the B to A ratio of the stoichiometries for the as-grown, etched, and ‘etched + annealed’ states. The data confirms the predominant A-site exposure in all the samples (B/A is always <1) and the increasing level of B site exposure with surface etching treatment. Hence, there is a gradual increase of B-site cations (notably Fe as shown in Fig. 3a) at the surface in the etched and ‘etched + annealed’ films. Importantly, while the surface is always A-site rich, it is observed that the predominantly A-site terminated surface from the as-grown films change to have both A- and B-site termination in the ‘etched + annealed’ films.

To corroborate the LEIS data, X-ray photoelectron spectroscopy (XPS) on as-grown (Figure S4 a), etched (Figure S4 a) and ‘etched +

annealed’ (Figure S4 b) films was performed. XPS can provide information related to the surface chemistry to volumes of ~1–3 nm³ from the surface [32]. This contrasts with LEIS, which looks only at the surface unit cells. The sub-surface regions of the as-grown sample show the typical Co 2p and Fe 2p spectra which contain the characteristic features of mixed Co²⁺ and Co³⁺ and Fe²⁺ and Fe³⁺ [33,34]. By comparing this data with LEIS (Fig. 2a), it is clear that Fe is present both at the surface (LEIS) and sub-surface (XPS) in the as-grown state. On the other hand, Co content was below the detection limit of the LEIS technique at the surface (Fig. 3a), but Co is present at the *sub-surface* (XPS, Figure S4 a) in the as-grown state.

Upon etching, while the Fe XPS spectrum does not show any substantial changes, indicating still a considerable presence of Fe²⁺ and Fe³⁺, the Co spectrum shows a reduced Co 2p signal (<60% of the intensity of the as-grown sample). This indicates that Co is etched out from the surface and/or sub-surface regions. Importantly, however, both XPS and LEIS techniques show that the content of Co at the surface and sub-surface is low upon etching. After annealing, the features of the Co 2p spectrum are partially recovered. This could indicate a thermally activated surface re-construction at the annealing conditions chosen (450 °C for 4 h), as also suggested by LEIS (Fig. 3a).

Fig. S4 (right-hand images) show XPS spectra for as-grown, etched (Figure S4 a) and ‘etched + annealed’ (Figure S4 b) films for the Fe 2p peaks. The features correspond to Fe²⁺ and Fe³⁺ cations. Unlike the Co XPS peaks, the Fe peaks show no clear decrease of Fe content with etching nor change in its surface oxidation state.

Subsequently, the determination of the oxygen exchange kinetics comparing 100LSCF thin-films with 50LSCF-50MgOVAN films for as-grown and ‘etched + annealed’ films is introduced. Fig. 4a shows the DC in-plane electric conductivity relaxation curves for as-grown and ‘etched + annealed’ samples. The representative data shown was taken at 400 °C, and show resistivity relaxation after changing the atmosphere

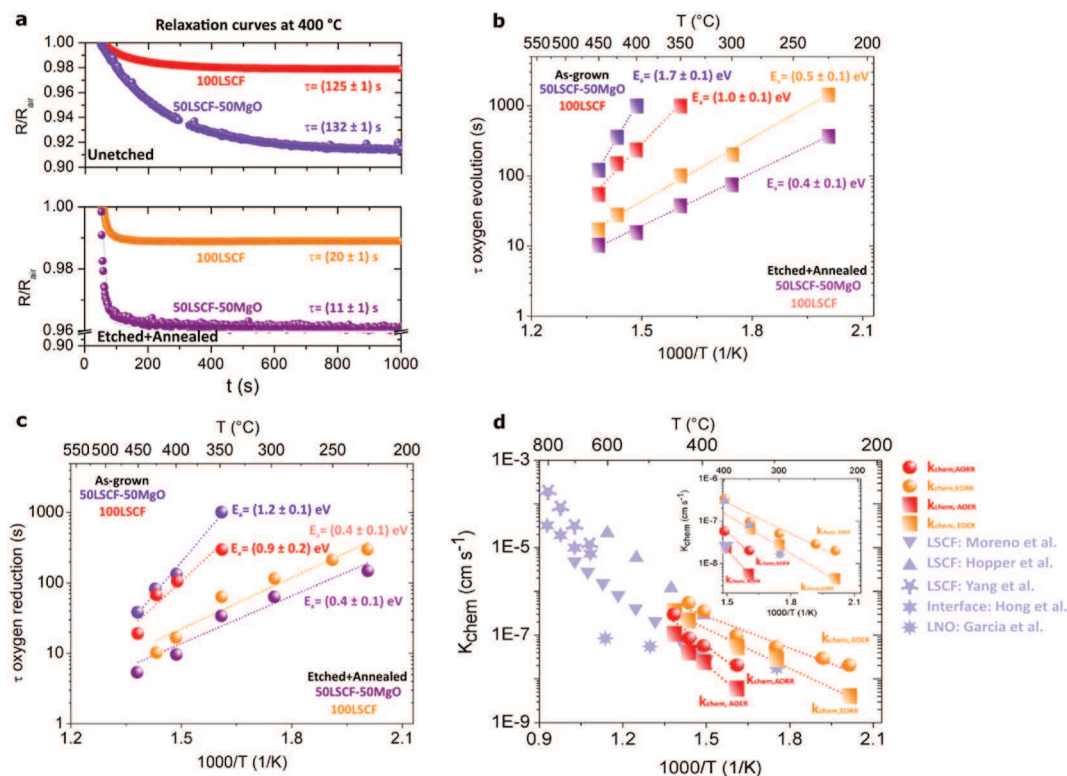


Fig. 4. DC conductivity relaxation for as-grown and etched + annealed 100LSCF and 50LSCF-50MgO. (a) Relaxation curves as a function of time obtained at 400 °C upon a fast change of atmosphere from air to oxygen. (b) and (c) show the relaxation time (c) as a function of $1000/T$ for films reduction and oxidation, respectively. (d) Calculated k_{chem} as a function of $1000/T$. All coefficients shown are described in the manuscript. Data from the literature are also presented for comparison purposes: LSCF: Moreno et al. [35], LSCF: Hopper et al. [36], LSCF: Yang et al. [37], Heterointerface: Hong et al. [38], and LNO: Garcia et al. [39].

from synthetic air to oxygen. The oxygen reduction reaction occurs and oxygen is exchanged from the atmosphere into the film (film oxidation). The change in conductivity as a function of time provides information on the oxygen reduction reaction kinetics. To describe the relaxation curves, fitting was done using a simple exponential law:

$$R(t) = R_{air} e^{-\frac{t}{\tau}} \quad (1)$$

where $R(t)$ is the resistivity at a given time t , R_{air} is the initial resistivity of the sample and τ is the characteristic time constant of relaxation.

Fig. 4a shows that the relaxation time τ for as-grown materials is (125 ± 1) s for 100LSCF compared to (132 ± 1) s for 50LSCF-50MgO. Etching + annealing dramatically enhances the kinetics for oxygen reduction by at least one order of magnitude compared to the as-grown state, resulting in τ of (20 ± 1) s and (11 ± 1) s for 100LSCF and 50LSCF-50MgO, respectively.

Fig. 4b and c shows the relaxation times obtained from measurements carried out from 450 °C to 200 °C during the oxidation and reduction, respectively. For both 100LSCF and 50LSCF-50MgO, τ shows the expected exponential temperature dependence in the as-grown and etched + annealed states, indicating a thermally activated process. For the as-grown samples, the oxidation process gives $E_a = (1.0 \pm 0.1)$ eV for 100LSCF and $E_a = (1.7 \pm 0.2)$ eV for 50LSCF-50MgO. Similar values (within the experimental errors) are obtained for the reduction process: $E_a = (0.9 \pm 0.2)$ eV for 100LSCF and $E_a = (1.2 \pm 0.1)$ eV for 50LSCF-50MgO.

The data is consistent with activation energies ranging between 0.7 eV and 1.2 eV, reported for oxygen reduction/oxidation processes for similar perovskite thin-films in literature [40,41]. The larger E_a for the oxygen exchange in 50LSCF-50MgO compared to 100LSCF or other perovskites in literature could result from the compression of LSCF by the MgO in the VAN [42] (see supplementary S1) and/or the presence of MgO at the reaction sites. A detailed explanation of this mechanism is beyond the scope of this manuscript.

The etched + annealed 100LSCF and 50LSCF-50MgO films show approximately the same activation energies for the exchange processes with a mean value of $E_a = (0.45 \pm 0.15)$ eV (Fig. 4b and c). This confirms that the intrinsic kinetic process is the same for 100LSCF and 50LSCF-50MgO in the etched + annealed state. Four material properties could play a role in determining the lower activation energy and fast kinetics for oxygen kinetics in etched materials compared to as-grown materials: out-of-plane strain, specific crystallographic planes at the surface, surface topography and/or surface chemistry effects. These possible effects are examined, one by one, below.

The strain effect on the oxygen exchange kinetics is a parameter only relevant for 50LSCF-50MgO as the strain of LSCF within the VAN changes upon etching (see discussion of Fig. 1, and supplementary S1). The lower activation energy and fast kinetics are featured in both etched 50LSCF-50MgO and etched 100LSCF. At the same time, in the latter, there is no strain variation upon etching (XRD of as-grown and etched LSCF are the same). This clarifies that strain is not responsible for the fast kinetics. Also, since both the VAN and the 100 LSCF thin-films are epitaxial and have the same (002) orientation (Fig. 1), the surface crystallography does not influence the activation energy or increase the kinetics of exchange upon etching + annealing.

The possible influence of surface topography effects on exchange kinetics is subsequently discussed. By comparing the etched 100LSCF (reference etched surface area) and etched 50LSCF-50MgO (same surface chemistry as reference 100LSCF but +239% increase in surface area), the role of the surface topography on the kinetics of oxygen exchange can be elucidated. Etched 100LSCF and etched 50LSCF-50MgO feature almost identical activation energies for oxygen exchange (mean value of $E_a = (0.45 \pm 0.15)$ eV as already noted and shown in Fig. 4b and c). Therefore, the first corollary is that the activation energy and, henceforth, the mechanism for oxygen exchange remains the same irrespective of the topography and surface area. However, it is observed

that the surface area does increase the exchange kinetics by decreasing the time constant for the relaxation kinetics by a factor that is comparable to the ratio between the exposed area and the projected (geometrical) area [43,44]. Hence, it was found that the relaxation times τ for etched 50LSCF-50MgO are 2–3 times lower than those of etched 100LSCF. This is consistent with increasing the solid/gas interface area to the geometrical area (+239%) obtained after MgO removal by etching. The remaining possible materials property responsible for explaining the extremely low mean activation energies for oxygen exchange $E_a = (0.45 \pm 0.15)$ eV and the very fast kinetics of the materials is surface chemistry [43].

Before discussing how the surface chemistry influences the oxygen exchange, it should be stressed the very high activity surface for oxygen exchange of etched materials at temperatures between 350 °C and 450 °C. For comparative purposes, the oxygen exchange coefficients, k_{chem} , determined from $\tau = l/k_{chem}$, where τ is the relaxation time (Fig. 4a) and l is the thin-film thickness are calculated. This calculation is not possible in the etched 50LSCF-50MgO film owing to its porosity. On the other hand, 100LSCF has a simple and well-defined planar geometry ($l = 70$ nm in this work). The determination of a single activation energy for observed oxygen exchange reduction/oxidation processes in the whole temperature regime, together with a low E_a value, allows us to exclude contributions from bulk oxygen diffusion in the exchange kinetics (typical activation energies for oxygen diffusion in LSCF ranges between 1.1 and 1.5 eV) [45–47]. Also, due to the substrate's inert nature (LSAT), any triple-phase boundary reaction could be discarded. Hence, the oxygen exchange occurs at the LSCF/gas interface for 100LSCF and the 50LSCF-50MgO.

Fig. 4d shows the calculated oxygen exchange coefficients for as-grown and etched 100LSCF ($k_{chem, AORR}$: exchange coefficient for oxygen reduction in as-grown 100LSCF; $k_{chem, EORR}$: exchange coefficient for oxygen reduction in etched + annealed 100LSCF; $k_{chem, AOER}$: exchange coefficient for oxygen evolution in as-grown 100LSCF, and $k_{chem, EOER}$: exchange coefficient for oxygen evolution in etched + annealed 100LSCF). Data of exchange coefficients on state-of-the-art thin-film cathode materials was also included [35–39]. The as-grown 100LSCF film features $k_{chem, AORR}$ and $k_{chem, AOER}$ with, within experimental error, the same values as reported in the literature [35,36]. This is seen by extrapolating our as-grown LSCF data in Fig. 4d to higher temperatures (see the overlap of data in this work and that for LSCF reported by Moreno et al. [35]). On the other hand, the etched + annealed 100LSCF films feature extremely fast kinetics for temperatures from 450 °C down to 300 °C. The values are over an order of magnitude faster than the as-grown films. Both $k_{chem, EORR}$ and $k_{chem, EOER}$ are exceptionally high and indicate that at temperatures from 300 °C to 450 °C, the kinetics for oxygen exchange (particularly reduction) in etched + annealed 100LSCF is faster than in $Ba_{0.5}Sr_{0.5}Co_{0.8}Fe_{0.2}O_{3-\delta}$ (BSCF) [48], $La_2NiO_{4-\delta}$ (LNO) [49], and complex heterointerfaces [11].

Subsequently, the influence of the surface chemistry on the oxygen exchange activation energy and kinetics is discussed. To estimate the correlation between the surface chemistry and the oxygen reduction kinetics, theoretical calculations using density functional theory with a linear combination of atomic orbitals (LCAO) were performed. To rationalize the finding, the main conclusions of the surface chemical analysis are first introduced, i.e. the etched + annealed material is characterized by a surface with much-increased B-site terminated (notably in Fe) fraction than the as-grown material, which featured a predominantly A-site terminated surface. It is well known that the Sr/LaO surfaces are less active than surfaces containing transition metals such as Co or Fe at the surface [5,14,50]. Based on these considerations, the calculations on a B-site terminated surface were investigated further. In other words, the focus was on understanding how such a surface might be driving the high electrochemical activity measured (Fig. 4). A qualitative description is provided by calculating the oxygen reduction in a model $La_{0.5}Sr_{0.5}Fe_{1-\beta}O_{3-\delta}$ (LSF) surface with (100) termination. Co is not included in the calculation because it is a qualitative approach, and

its experimentally measured low content (Fig. 3a and Supp 4). This also allowed the model to be created with a computationally manageable size due to reduced composition complexity. Also, since it has been experimentally shown that oxygen vacancies are abundant at perovskite surfaces [51], and high vacancy concentrations are expected in B-site terminated perovskites [5], the oxygen reduction at the LSF surface with a different surface oxygen vacancy content was investigated further. To keep charge neutrality at the LSF surface, surface oxygen vacancies could either be compensated electronically or by cation vacancies. No changes in chemical oxidation states of the cation species were observed using XPS (Supp 4), and hence it can be assumed that the surface electronic states of the cations did not change with etching or annealing. Therefore, it is assumed that charge compensation of oxygen vacancies occurs with cation vacancies.

Based on these considerations, Fig. 5a shows two exemplary oxygen dissociation processes at LSF Fe–O terminated surfaces that can qualitatively describe the experimental conditions. Two different defect structures determine the two conditions: represented in red, the calculations were made for a surface with a cation-defect-free surface and 2 surface O defect sites. Represented in blue, the calculations were made for a surface with 1 Fe cation vacancy and 4 O vacancy sites. For both surface defect structures, the O₂ dissociation steps are schematically represented. Fig. 5b and c shows the i) O₂ adsorption process; ii) O₂ transition state during dissociation with its corresponding activation

energy; and iii) final O₂ dissociated state with its corresponding activation energy compared to the initial state when O₂ was adsorbed for each surface structure.

The first step in both processes is the O₂ adsorption step (Fig. 5b i and Fig. 5c i), followed by a transition during the dissociation. The transition step during the dissociation of an adsorbed O₂ molecule at two surface O defect sites has an energy barrier of 1.01 eV (Fig. 5b ii). This energy barrier is expected in perovskites [40,41]. Upon calculating the energy for the transition step during the dissociation of an adsorbed O₂ molecule at 4 surface O defect sites and 1 compensating surface Fe defect (Fig. 5c ii), it is found that the energy barrier reduces considerably to 0.36 eV. Such a strong decrease in the energy barrier for oxygen reduction is consistent with our experimental observations for the etched materials. The higher activity due to increased oxygen vacancy concentration is consistent with theoretical literature studies [5].

The final state of the upper and lower exemplary cases shows the final dissociation of oxygen. Upon completing the oxygen reduction, the case with two surface O vacancies has a relative energy stability of –0.016 eV compared to the initial state (Fig. 5b iii). The case with 4 surface O defect sites and 1 surface Fe vacancy has a relative energy stability of –1.14 eV compared to its initial state (Fig. 5c iii). The latter implies that the dissociated state of the oxygen atoms is significantly favoured at the highly defective surface. This also implies that the reverse of the ORR reaction is unlikely at this surface or, in other words,

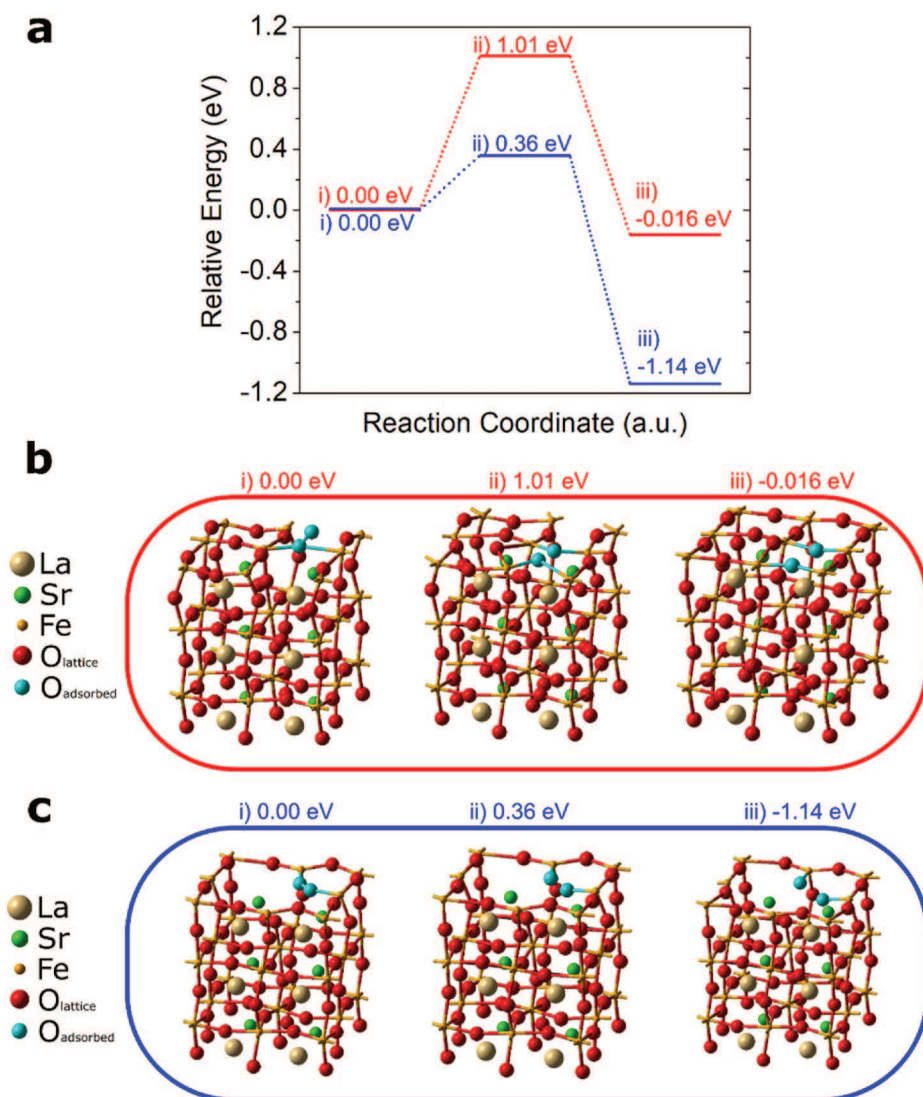


Fig. 5. a) calculated O₂ dissociation steps and their relative energies for ORR taking place at two different Fe–O terminated (001) La_{0.5}Sr_{0.5}Fe_{1- β} O_{3- δ} surfaces. The calculation was made for b) a cation-defect-free surface and two surface O vacancies. As shown in red, the transition state has a barrier of 1.01 eV, and the final energy barrier is –0.016 eV. In c), the calculations are shown for a surface with 1 surface Fe vacancy and 4 surface O vacancies. In blue, it is observed that the transition state has a barrier 0.36 eV, and the final energy barrier is –1.14 eV. (For interpretation of the references to colour in this figure legend, the reader is referred to the Web version of this article.)

that the oxygen reduction is indeed thermodynamically favoured. The result, therefore, correlates very well with our experimental observations for oxygen reduction in Fig. 3b and c and, in particular, allows us to appreciate how the high oxygen vacancy concentration might reduce the oxygen dissociation barrier, which is generally considered to be one of the critical steps in the oxygen surface exchange.

The calculations also provide a further detailed understanding of the oxygen reduction reaction when comparing the surfaces with different defect states (i.e., comparing the surface with two O vacancy sites and the surface with 4 O vacancy sites and 1 Fe vacancy). For both cases, the O–O bond lengths (1.329 Å and 1.320 Å, respectively) of the adsorbed O₂ and its Mulliken electron densities suggest that the O₂ has been activated to the superoxo O₂⁻ state. However, the dissociation barriers are quite different for the different defect surfaces. Essentially, the extra oxygen vacancies at the surface can act as electron donors and increase the local charge density of the surface metal atoms, which allows them to donate electrons more readily to the incoming O₂ molecules and help O₂ dissociation. Indeed, the average Mulliken charge densities of the surface Fe atoms calculated in the Fe + O defect case is 24.175 eV, higher than the value (24.052 eV) calculated for the case with only 2 O defect sites. Surface oxygen defect engineering has been regarded as an important way to enhance the ORR reaction activity of solid oxide catalysts. An increased surface oxygen defect concentration has been responsible for improved oxygen reduction activities in simple oxides [52–54].

Overall, in this work, the combination of surface chemical modification and microstructure engineering leading to a mesoporous surface yields an unprecedented electrochemical performance of LSCF cathode thin film. Together with the simple fabrication of one-step film growth plus room-temperature chemical etching, our approach shows a new direction for enhancing the oxygen reduction reaction for lower temperature operation of micro solid-oxide cells and membranes. Indeed, the next step would be to investigate integrating these materials into a processing route that would allow them to be produced [55,56]. Future works may also evaluate whether such a simple etching technique could be replicated in other bulk materials.

4. Conclusions

In this work, both epitaxial (100) LSCF and vertically aligned nanocomposites comprised of (100) LSCF+(100) MgO were synthesized. It is shown that a simple room-temperature post-processing etching can obtain a remarkably active surface with 20 vol % acetic acid. The process gives rise to extremely fast oxygen exchange at operational temperatures between 350 °C and 450 °C in (La_{0.60}Sr_{0.40})_{0.95}(Co_{0.20}Fe_{0.80})O₃ (LSCF) single-phase and 50 wt% LSCF films and 50 wt% MgO vertically aligned nanocomposites. It is demonstrated that etching (100) LSCF changes from a predominantly A-site termination surface to one with mixed A- and B-site termination. More than an order of magnitude increase of the oxygen exchange kinetics at temperatures between 300 °C and 450 °C with the mixed A- and B-site terminated surface was achieved, and activation energies for oxygen exchange as low as 0.4 eV. The latter is half of the activation energy value for the predominantly A-site terminated as-grown material. The same etching procedure in the nanocomposite films gives also rise to an interconnected honeycomb-like porous nanostructure of (100) LSCF with maximized mesoporosity (~200% area increase for <100 nm thin-films) which increases the oxygen exchange kinetics by a factor that is proportional to this solid/gas interface area increase. DFT calculations confirmed the experimental findings. Hence, Fe-terminated surfaces of LSCF with additional oxygen vacancies that compensate for cation deficiency explain the ultrafast oxygen exchange kinetics obtained. Overall, this study shows a simple way of creating new surface compositions of cathode materials for solid electrolytic cells to achieve cathode kinetics, reaching the goals needed for solid oxide energy devices to work below 500 °C.

CRedit authorship contribution statement

Matias Acosta: Experiments were conceived, Sample preparation was carried out, SEM characterization, XRD: Sample preparation was carried out, AFM: Sample preparation was carried out and electrochemical characterization, calculations were done. Designed and coordinated the research plan and prepared the initial draft that was discussed. **Federico Baiutti:** Experiments were conceived, electrochemical characterization was done. **Xuejing Wang and Haiyan Wang:** TEM characterization. **Andrea Cavallaro and Ainara Aguadero:** LEIS characterization and calculations were done. **Weiwei Li:** XPS characterization, calculations were done. **Ji Wu and Stephen C. Parker:** theoretical calculations were done. **Judith L. MacManus-Driscoll:** Experiments were conceived, co-designed and supported the research plan and the initial draft. All the authors contributed to the interpretation and discussion of the experimental data, and, to edit the working drafts.

Declaration of competing interest

The authors declare that they have no known competing financial interests or personal relationships that could have appeared to influence the work reported in this paper.

Acknowledgments

M.A. acknowledges the support from the Feodor Lynen Research Fellowship Program of the Alexander von Humboldt Foundation and the Isaac Newton Trust, minute 17.25(a). M.A. and J.L/M.D. acknowledge the support from the EPSRC Centre of Advanced Materials for Integrated Energy Systems (CAM-IES) under EP/P007767/1 and the Royal Academy of Engineering Chair in Emerging Technologies, grant CIET1819_24, and EPSRC grant EP/T012218/1. Part of this work has been funded by the European Union's Horizon 2020 research and innovation programme under grant agreement No 824072 (Harvestore) and no. 10101017709 (Epistore) and by an STSM Grant from the COST Action MP1308: Towards Oxide-Based Electronics (TO-BE), supported by COST (European Cooperation in Science and Technology). A.T. acknowledges the support of the Generalitat de Catalunya-AGAUR (2017 SGR 1421). A.A and A.C acknowledge the support of EPSRC ICSF North East Centre for Energy Materials research hub EP/R023581/1 and EPSRC JSPS Core to Core "Solid Oxide Interfaces for Faster Ion Transport (SOIFIT)" EP/P026478/1. X.W. and H.W. acknowledge the funding support from the U.S. National Science Foundation for the TEM effort at Purdue University (DMR-2016453 and ECCS-1902644). J.W. and S.C.P. acknowledge the support from the EPSRC (EP/P007821/1 and EP/R023603/1). J.W and S.C.P. would also like to thank the U.K. Archer HPC facility for providing computation resources, accessed through the U.K. Materials Chemistry Consortium (funded by the EPSRC grants: EP/L000202, EP/R029431, EP/T022213). This research has also used the Balena High-Performance Computing (HPC) Service at the University of Bath.

Appendix A. Supplementary data

Supplementary data to this article can be found online at <https://doi.org/10.1016/j.jpowsour.2022.230983>.

References

- [1] Y. Chen, W. Zhou, D. Ding, M. Liu, F. Ciucci, M. Tade, Z. Shao, Advances in cathode materials for solid oxide fuel cells: complex oxides without Alkaline earth metal elements, *Adv. Energy Mater.* 5 (2015) 1500537, <https://doi.org/10.1002/aenm.201500537>.
- [2] T.M. Gür, Comprehensive review of methane conversion in solid oxide fuel cells: prospects for efficient electricity generation from natural gas, *Prog. Energy Combust. Sci.* 54 (2016) 1–64, <https://doi.org/10.1016/j.pecs.2015.10.004>.

- [3] Y. Zhang, R. Knibbe, J. Sunarso, Y. Zhong, W. Zhou, Z. Shao, Z. Zhu, Recent progress on advanced materials for solid-oxide fuel cells operating below 500 °C, *Adv. Mater.* 29 (2017) 1700132, <https://doi.org/10.1002/adma.201700132>.
- [4] M.M. Kulkija, E.A. Kotomin, Y. Merkle, Y.A. Mastrikov, J. Maier, Combined theoretical and experimental analysis of processes determining cathode performance in solid oxide fuel cells, *Phys. Chem. Chem. Phys.* 15 (2013) 5443–5471, <https://doi.org/10.1039/C3CP44363A>.
- [5] Y. Cao, M.J. Gadre, A.T. Ngo, S.B. Adler, D.D. Morgan, Factors controlling surface oxygen exchange in oxides, *Nat. Commun.* 10 (2019) 1346, <https://doi.org/10.1038/s41467-019-08674-4>.
- [6] H. Kusaba, Y. Shibata, K. Sasaki, Y. Teraoka, Surface effect on oxygen permeation through dense membrane of mixed-conductive LSCF perovskite-type oxide, *Solid State Ionics* 177 (2006) 2249–2253, <https://doi.org/10.1016/j.ssi.2006.05.038>.
- [7] N. Tsvetkov, Q. Lu, L. Sun, E.J. Crumlin, B. Yildiz, Improved chemical and electrochemical stability of perovskite oxides with less reducible cations at the surface, *Nat. Mater.* 15 (2016) 1010–1016, <https://doi.org/10.1038/nmat4659>.
- [8] M. Riva, M. Kubicek, X. Hao, G. Franceschi, S. Gerhold, M. Schmid, H. Hutter, J. Fleig, C. Franchini, B. Yildiz, U. Diebold, Influence of surface atomic structure demonstrated on oxygen incorporation mechanism at a model perovskite oxide, *Nat. Commun.* 9 (2018), <https://doi.org/10.1038/s41467-018-05685-5>.
- [9] S.B. Adler, J.A. Lane, B.C.H. Steele, Electrode kinetics of porous mixed-conducting oxygen electrodes, *J. Electrochem. Soc.* 143 (1996) 3554–3564, <https://doi.org/10.1149/1.1837252>.
- [10] M. Acosta, F. Baiutti, A. Tarancón, J.L. MacManus-Driscoll, Nanostructured materials and interfaces for advanced ionic electronic conducting oxides, *Adv. Mater. Interfac.* (2019) 1900462, <https://doi.org/10.1002/admi.201900462>.
- [11] T. Hong, L. Zhang, F. Chen, C. Xia, Oxygen surface exchange properties of La_{0.6}Sr_{0.4}Co_{0.8}Fe_{0.2}O_{3-δ} coated with SmxCe_{1-x}O_{2-δ}, *J. Power Sources* 218 (2012) 254–260, <https://doi.org/10.1016/j.jpowsour.2012.07.004>.
- [12] G.M. Rupp, H. Tézé, J. Druce, A. Limbeck, T. Ishihara, J. Kilner, J. Fleig, Surface chemistry of La_{0.6}Sr_{0.4}Co_{3-δ} thin-films and its impact on the oxygen surface exchange resistance, *J. Mater. Chem.* 3 (2015) 22759–22769, <https://doi.org/10.1039/C5TA05279C>.
- [13] Z. Cai, M. Kubicek, J. Fleig, B. Yildiz, Chemical heterogeneities on La_{0.6}Sr_{0.4}CoO_{3-δ} thin-films—correlations to cathode surface activity and stability, *Chem. Mater.* 24 (2012) 1116–1127, <https://doi.org/10.1021/cm203501u>.
- [14] G.M. Rupp, A.K. Opitz, A. Nennung, A. Limbeck, J. Fleig, Real-time impedance monitoring of oxygen reduction during surface modification of thin film cathodes, *Nat. Mater.* 16 (2017) 640–645, <https://doi.org/10.1038/nmat4879>.
- [15] A.K. Opitz, C. Rameshan, M. Kubicek, G.M. Rupp, A. Nennung, T. Götsch, R. Blume, M. Hävecker, A. Knop-Gericke, G. Rupprechter, B. Klötzer, J. Fleig, The chemical evolution of the La_{0.6}Sr_{0.4}CoO_{3-δ} surface under SOFC operating conditions and its implications for electrochemical oxygen exchange activity, *Top. Catal.* 61 (2018) 2129–2141, <https://doi.org/10.1007/s11244-018-1068-1>.
- [16] W. Jung, H.L. Tuller, Investigation of surface Sr segregation in model thin film solid oxide fuel cell perovskite electrodes, *Energy Environ. Sci.* 5 (2012) 5370–5378, <https://doi.org/10.1039/C1EE02762J>.
- [17] B. Koo, K. Kim, J.K. Kim, H. Kwon, J.W. Han, W. Jung, Sr segregation in perovskite oxides: why it happens and how it exists, *Joule* 2 (2018) 1476–1499, <https://doi.org/10.1016/j.joule.2018.07.016>.
- [18] A. Staykov, S. Fukumori, K. Yoshizawa, K. Sato, T. Ishihara, J. Kilner, Interaction of SrO-terminated SrTiO₃ surface with oxygen, carbon dioxide, and water, *J. Mater. Chem. A.* 6 (2018) 22662–22672, <https://doi.org/10.1039/C8TA05177A>.
- [19] M. Kubicek, A. Limbeck, T. Frömling, H. Hutter, J. Fleig, Relationship between cation segregation and the electrochemical oxygen reduction kinetics of La_{0.6}Sr_{0.4}CoO_{3-δ} thin film electrodes, *J. Electrochem. Soc.* 158 (2011) B727, <https://doi.org/10.1149/1.3581114>.
- [20] M. Kubicek, G.M. Rupp, S. Huber, A. Penn, A.K. Opitz, J. Bernardi, M. Stöger-Pollach, H. Hutter, J. Fleig, Cation diffusion in La_{0.6}Sr_{0.4}CoO_{3-δ} below 800 °C and its relevance for Sr segregation, *Phys. Chem. Chem. Phys.* 16 (2014) 2715, <https://doi.org/10.1039/c3cp51906f>.
- [21] H.H. Brongersma, M. Draxler, M. de Ridder, P. Bauer, Surface composition analysis by low-energy ion scattering, *Surf. Sci. Rep.* 62 (2007) 63–109, <https://doi.org/10.1016/j.surfrep.2006.12.002>.
- [22] C.T. Rueden, J. Schindelin, M.C. Hiner, B.E. DeZonia, A.E. Walter, E.T. Arena, K. W. Eliceiri, ImageJ2: ImageJ for the next generation of scientific image data, *BMC Bioinform.* 18 (2017) 529, <https://doi.org/10.1186/s12859-017-1934-z>.
- [23] M.W. den Otter, H.J.M. Bouwmeester, B.A. Boukamp, H. Verweij, Reactor flush time correction in relaxation experiments, *J. Electrochem. Soc.* 148 (2001) J1, <https://doi.org/10.1149/1.1337604>.
- [24] R. Dovesi, A. Erba, R. Orlando, C.M. Zicovich-Wilson, B. Civalleri, L. Maschio, M. Rérat, S. Casassa, J. Baima, S. Salustro, B. Kirtman, Quantum-mechanical condensed matter simulations with CRYSTAL, WIREs Computational Molecular Science 8 (2018), e1360, <https://doi.org/10.1002/wcms.1360>.
- [25] B.G. Searle, D.L. Visualize, *Comput. Phys. Commun.* 137 (2001) 25–32, [https://doi.org/10.1016/S0010-4655\(01\)00170-9](https://doi.org/10.1016/S0010-4655(01)00170-9).
- [26] E. Heifets, E.A. Kotomin, A.A. Bagatyrants, J. Maier, Thermodynamic stability of non-stoichiometric SrFeO_{3-δ}: a hybrid DFT study, *Phys. Chem. Chem. Phys.* 21 (2019) 3918–3931, <https://doi.org/10.1039/C8CP07117A>.
- [27] J. Wu, S.S. Pramana, S.J. Skinner, J.A. Kilner, A.P. Horsfield, Why Ni is absent from the surface of La₂NiO_{4+δ}, *J. Mater. Chem.* 3 (2015) 23760–23767, <https://doi.org/10.1039/C5TA03759J>.
- [28] M. Dolg, H. Stoll, A. Savin, H. Preuss, Energy-adjusted pseudopotentials for the rare earth elements, *Theor. Chim. Acta* 75 (1989) 173–194, <https://doi.org/10.1007/BF00528565>.
- [29] K. Okhotnikov, T. Charpentier, S. Cadars, Supercell program: a combinatorial structure-generation approach for the local-level modeling of atomic substitutions and partial occupancies in crystals, *J. Cheminf.* 8 (2016) 17, <https://doi.org/10.1186/s13321-016-0129-3>.
- [30] A. Rimola, C.M. Zicovich-Wilson, R. Dovesi, P. Ugliengo, Search and characterization of transition state structures in crystalline systems using valence Coordinates, *J. Chem. Theor. Comput.* 6 (2010) 1341–1350, <https://doi.org/10.1021/ct900680f>.
- [31] P.A. Stampe, R.J. Kennedy, X-ray characterization of MgO thin-films grown by laser ablation on SrTiO₃ and LaAlO₃, *J. Cryst. Growth* 191 (1998) 478–482, [https://doi.org/10.1016/S0022-0248\(98\)00217-6](https://doi.org/10.1016/S0022-0248(98)00217-6).
- [32] M.P. Seah, W.A. Dench, Quantitative electron spectroscopy of surfaces: a standard data base for electron inelastic mean free paths in solids, *Surf. Interface Anal.* 1 (1979) 2–11, <https://doi.org/10.1002/sia.740010103>.
- [33] L. Qiao, H.Y. Xiao, H.M. Meyer, J.N. Sun, C.M. Rouleau, A.A. Puzos, D. B. Geohegan, L.N. Ivanov, M. Yoon, W.J. Weber, M.D. Biegalski, Nature of the band gap and origin of the electro-/photo-activity of Co₃O₄, *J. Mater. Chem. C.* 1 (2013) 4628–4633, <https://doi.org/10.1039/C3TC30861H>.
- [34] M. Descostes, F. Mercier, N. Thomat, C. Beaucaire, M. Gautier-Soyer, Use of XPS in the determination of chemical environment and oxidation state of iron and sulfur samples: constitution of a data basis in binding energies for Fe and S reference compounds and applications to the evidence of surface species of an oxidized pyrite in a carbonate medium, *Appl. Surf. Sci.* 165 (2000) 288–302, [https://doi.org/10.1016/S0169-4332\(00\)00443-8](https://doi.org/10.1016/S0169-4332(00)00443-8).
- [35] R. Moreno, J. Zapata, J. Roqueta, N. Bagnés, J. Santiso, Chemical strain and oxidation-reduction kinetics of epitaxial thin-films of mixed ionic-electronic conducting oxides determined by X-ray diffraction, *J. Electrochem. Soc.* 161 (2014) F3046–F3051, <https://doi.org/10.1149/2.0091411jes>.
- [36] E.M. Hopper, E. Perret, B.J. Ingram, H. You, K.-C. Chang, P.M. Baldo, P.H. Fuoss, J. A. Eastman, Oxygen exchange in La_{0.6}Sr_{0.4}Co_{0.2}Fe_{0.8}O_{3-δ} thin-film heterostructures under applied electric potential, *J. Phys. Chem. C* 119 (2015) 19915–19921.
- [37] Y. Yang, M. Li, Y. Ren, Y. Li, C. Xia, Magnesium oxide as synergistic catalyst for oxygen reduction reaction on strontium doped lanthanum cobalt ferrite, *Int. J. Hydrogen Energy* 43 (2018) 3797–3802, <https://doi.org/10.1016/j.ijhydene.2017.12.183>.
- [38] T. Hong, M. Zhao, K. Brinkman, F. Chen, C. Xia, Enhanced oxygen reduction activity on ruddlesden–popper phase decorated La_{0.8}Sr_{0.2}FeO_{3-δ} 3D heterostructured cathode for solid oxide fuel cells, *ACS Appl. Mater. Interfaces* 9 (2017) 8659–8668, <https://doi.org/10.1021/acsami.6b14625>.
- [39] G. Garcia, M. Burriel, N. Bonanos, J. Santiso, Electrical conductivity and oxygen exchange kinetics of La₂NiO_{4+δ} thin-films grown by chemical vapor deposition, *J. Electrochem. Soc.* 155 (2008) P28, <https://doi.org/10.1149/1.2829900>.
- [40] C.C. Kan, E.D. Wachsmann, Isotopic-switching analysis of oxygen reduction in solid oxide fuel cell cathode materials, *Solid State Ionics* 181 (2010) 338–347, <https://doi.org/10.1016/j.ssi.2009.12.011>.
- [41] N.J. Simrick, A. Bieberle-Hütter, T.M. Ryll, J.A. Kilner, A. Atkinson, J.L.M. Rupp, An investigation of the oxygen reduction reaction mechanism of La_{0.6}Sr_{0.4}Co_{0.2}Fe_{0.8}O₃ using patterned thin-films, *Solid State Ionics* 206 (2012) 7–16, <https://doi.org/10.1016/j.ssi.2011.10.029>.
- [42] S. Lee, W. Zhang, F. Khatkhatay, Q. Jia, H. Wang, J.L. MacManus-Driscoll, Strain tuning and strong enhancement of ionic conductivity in SrZrO₃-RE₂O₃ (RE = Sm, Eu, Gd, Dy, and Er) nanocomposite films, *Adv. Funct. Mater.* 25 (2015) 4328–4333, <https://doi.org/10.1002/adfm.201404420>.
- [43] M. Mosleh, M. Søgaard, P.V. Hendriksen, Kinetics and mechanisms of oxygen surface exchange on La_{0.6}Sr_{0.4}FeO_{3-δ} thin-films, *J. Electrochem. Soc.* 156 (2009) B441, <https://doi.org/10.1149/1.3062941>.
- [44] Y. Lu, C. Kreller, S.B. Adler, Measurement and modeling of the impedance characteristics of porous La_{1-x}Sr_xCoO_{3-δ} electrodes, *J. Electrochem. Soc.* 156 (2009) B513, <https://doi.org/10.1149/1.3079337>.
- [45] L.M. van der Haar, M.W. den Otter, M. Morskate, H.J.M. Bouwmeester, H. Verweij, Chemical diffusion and oxygen surface transport of La_{1-x}Sr_xCoO_{3-δ} studied with electrical conductivity relaxation, *J. Electrochem. Soc.* 149 (2002) J41, <https://doi.org/10.1149/1.1446874>.
- [46] D. Tripković, R. Küngas, M.B. Mogensén, P.V. Hendriksen, Surface recrystallization – an underestimated phenomenon affecting oxygen exchange activity, *J. Mater. Chem. A.* 7 (2019) 11782–11791, <https://doi.org/10.1039/C9TA02607J>.
- [47] F. Monaco, V. Tezyk, E. Siebert, S. Pylypko, B. Morel, J. Vulliet, T. Le Bihan, F. Lefebvre-Joud, J. Laurencin, Experimental validation of a La_{0.6}Sr_{0.4}Co_{0.2}Fe_{0.8}O_{3-δ} electrode model operated in electrolysis mode: understanding the reaction pathway under anodic polarization, *Solid State Ionics* 319 (2018) 234–246, <https://doi.org/10.1016/j.ssi.2018.02.012>.
- [48] M. Burriel, C. Niedrig, W. Menesklou, S.F. Wagner, J. Santiso, E. Ivers-Tiffée, BSCF epitaxial thin-films: electrical transport and oxygen surface exchange, *Solid State Ionics* 181 (2010) 602–608, <https://doi.org/10.1016/j.ssi.2010.03.005>.
- [49] G. Garcia, M. Burriel, N. Bonanos, J. Santiso, Electrical conductivity and oxygen exchange kinetics of La₂NiO_{4+δ} thin films grown by chemical vapor deposition, *J. Electrochem. Soc.* 155 (2008) P28, <https://doi.org/10.1149/1.2829900>.
- [50] X. Wang, X. Li, X. Chu, R. Cao, J. Qian, Y. Cong, K. Huang, J. Wang, C. Redshaw, R. Sarangi, G. Li, S. Feng, Manipulating surface termination of perovskite manganate for oxygen activation, *Adv. Funct. Mater.* 31 (2021) 2006439, <https://doi.org/10.1002/adfm.202006439>.
- [51] F. Gunkel, D.V. Christensen, Y.Z. Chen, N. Pryds, Oxygen vacancies: the (in)visible friend of oxide electronics, *Appl. Phys. Lett.* 116 (2020) 120505, <https://doi.org/10.1063/1.5143309>.

- [52] D.A. Tompsett, S.C. Parker, M.S. Islam, Rutile (β -)MnO₂ surfaces and vacancy formation for high electrochemical and catalytic performance, *J. Am. Chem. Soc.* 136 (2014) 1418–1426, <https://doi.org/10.1021/ja4092962>.
- [53] C.T. Campbell, C.H.F. Peden, Oxygen vacancies and catalysis on ceria surfaces, *Science* 309 (2005) 713–714, <https://doi.org/10.1126/science.1113955>.
- [54] S. Sun, M. Watanabe, J. Wu, Q. An, T. Ishihara, Ultrathin WO₃-0.33H₂O nanotubes for CO₂ photoreduction to acetate with high selectivity, *J. Am. Chem. Soc.* 140 (2018) 6474–6482, <https://doi.org/10.1021/jacs.8b03316>.
- [55] I. Garbayo, D. Pla, A. Morata, L. Fonseca, N. Sabaté, A. Tarancón, Full ceramic micro solid oxide fuel cells: towards more reliable MEMS power generators operating at high temperatures, *Energy Environ. Sci.* 7 (2014) 3617–3629, <https://doi.org/10.1039/C4EE00748D>.
- [56] M.P. Wells, A.J. Lovett, T. Chalklen, F. Baiutti, A. Tarancón, X. Wang, J. Ding, H. Wang, S. Kar-Narayan, M. Acosta, J.L. MacManus-Driscoll, Route to high-performance micro-solid oxide fuel cells on metallic substrates, *ACS Appl. Mater. Interfaces* 13 (2021) 4117–4125, <https://doi.org/10.1021/acsami.0c15368>.